


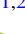


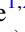





3-OGC: Catalog of Gravitational Waves from Compact-binary Mergers

Alexander H. Nitz^{1,2} , Collin D. Capano^{1,2} , Sumit Kumar^{1,2} , Yi-Fan Wang (王一帆)^{1,2} , Shilpa Kastha^{1,2} ,
Marlin Schäfer^{1,2} , Rahul Dhurkunde^{1,2} , and Miriam Cabero³ 

¹Max-Planck-Institut für Gravitationsphysik (Albert-Einstein-Institut), D-30167 Hannover, Germany; alex.nitz@aei.mpg.de

²Leibniz Universität Hannover, D-30167 Hannover, Germany

³Department of Physics and Astronomy, The University of British Columbia, Vancouver, BC V6T 1Z4, Canada

Received 2021 May 27; revised 2021 August 2; accepted 2021 August 8; published 2021 November 23

Abstract

We present the third open gravitational-wave catalog (3-OGC) of compact-binary coalescences, based on the analysis of the public LIGO and Virgo data from 2015 through 2019 (O1, O2, O3a). Our updated catalog includes a population of 57 observations, including 4 binary black hole mergers that had not been previously reported. This consists of 55 binary black hole mergers and the 2 binary neutron star mergers, GW170817 and GW190425. We find no additional significant binary neutron star or neutron star–black hole merger events. The most confident new detection is the binary black hole merger GW190925_232845, which was observed by the LIGO–Hanford and Virgo observatories with $\mathcal{P}_{\text{astro}} > 0.99$; its primary and secondary component masses are $20.2_{-2.5}^{+3.9} M_{\odot}$ and $15.6_{-2.6}^{+2.1} M_{\odot}$, respectively. We estimate the parameters of all binary black hole events using an up-to-date waveform model that includes both subdominant harmonics and precession effects. To enable deep follow up as our understanding of the underlying populations evolves, we make available our comprehensive catalog of events, including the subthreshold population of candidates, and the posterior samples of our source parameter estimates.

Unified Astronomy Thesaurus concepts: [Gravitational waves \(678\)](#); [Neutron stars \(1108\)](#); [Astrophysical black holes \(98\)](#); [Gravitational wave astronomy \(675\)](#)

1. Introduction

With the advent of the current generation of interferometric gravitational-wave detectors, the observation of gravitational waves from the coalescence of compact-binary mergers has become a regular and rapidly maturing component of astronomy. The Advanced LIGO (Aasi et al. 2015) and Advanced Virgo (Acernese et al. 2015) observatories have now been observing at high sensitivity since 2015 and 2017, respectively. During this period they have completed three observing runs (O1–O3). Dozens of binary black hole (BBH) mergers have been reported from these observing runs, in addition to a handful of binary neutron star (BNS) coalescences (Nitz et al. 2019d; Venumadhav et al. 2020a; Abbott et al. 2019b, 2021b, 2020a, 2017a). Notably, GW170817 remains the sole observation with unambiguous electromagnetic counterparts (Abbott et al. 2017b, 2017a). Novel observations such as the massive GW190521 merger (Abbott et al. 2020c) are starting to challenge our models of stellar formation (Abbott et al. 2020d; Edelman et al. 2021; Gerosa & Fishbach 2021; Zevin et al. 2021) and are pushing the limits of gravitational waveform modeling (Gayathri et al. 2020; Romero-Shaw et al. 2020; Estellés et al. 2021).

In this work, we provide a comprehensive catalog of gravitational waves from the coalescence of BNS, neutron star–black hole (NSBH), and BBH systems based on a deep archival search for compact-binary mergers of the public LIGO and Virgo data (Vallisneri et al. 2015; Abbott et al. 2021a). The previous open gravitational-wave catalog (2-OGC) searched for the signature of compact-binary mergers in the O1 and O2 observing runs. We re-analyze the entirety of the public LIGO and Virgo data comprised of O1, O2, and the recently published O3a data set (Vallisneri et al. 2015; Abbott et al. 2021a), which covers the first

half, from 1 April to 1 October of 2019, of the concluded O3 observing run. The O3 data is being released in six-month chunks, with O3a being the first; the second half is expected in six months time. Included in our data release is the complete set of subthreshold candidates in addition to posterior samples from estimates of the most significant mergers. Subthreshold candidates can be correlated with archival observations (e.g., from gamma-ray bursts, Burns et al. 2019; Nitz et al. 2019c; high-energy neutrinos, Countryman et al. 2019; or optical transients, Andreoni et al. 2019; Setzer et al. 2019) to potentially uncover fainter, distant populations.

We improve the sensitivity of our analysis over our previous catalog search by targeted use of signal consistency tests, updated data cleaning procedures, and stricter allowance for loss in signal-to-noise ratios (S/Ns). As in 2-OGC, for candidates consistent with the bulk of the increasing population of observed BBH mergers, we estimate the probability of astrophysical origin using the focused BBH region of our larger search. This estimate takes into account the measured rate of mergers and the possibly confounding background noise. Additionally, for the first time in this catalog, we incorporate BNS and BBH candidates observed by a single sensitive detector using methods introduced in Nitz et al. (2020).

We find that 55 BBH mergers have been observed from 2015–2019 along with 2 BNS mergers. These include four BBH mergers from the O3a period that had not been previously reported. Our results are broadly consistent with the cumulative sum of previous catalogs (Abbott et al. 2019b; Nitz et al. 2019a, 2019d; Venumadhav et al. 2020a), including the recent analysis of O3a by the LIGO–Virgo–Kagra Collaboration (Abbott et al. 2021b).

2. LIGO and Virgo Observing Periods

We analyze the complete set of public LIGO and Virgo data from the O1, O2, and O3a observing runs (Vallisneri et al. 2015;



Original content from this work may be used under the terms of the [Creative Commons Attribution 4.0 licence](#). Any further distribution of this work must maintain attribution to the author(s) and the title of the work, journal citation and DOI.

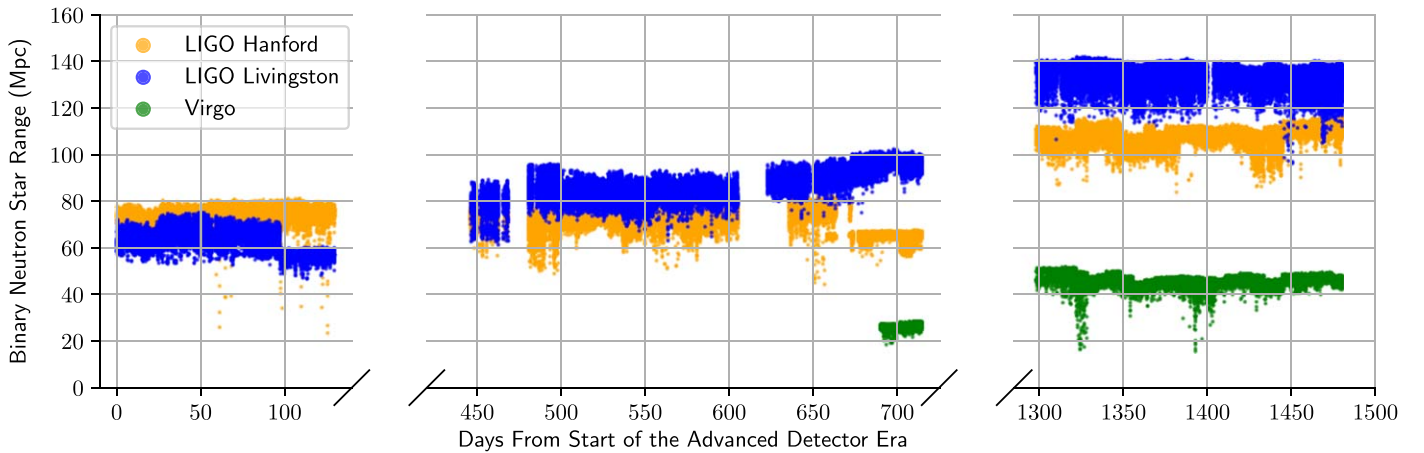


Figure 1. The sky and orientation averaged distance that a fiducial $1.4\text{--}1.4 M_{\odot}$ BNS merger can be observed by the LIGO–Hanford (yellow), LIGO–Livingston (blue), and Virgo (green) observatories at an S/N of 8. The O1 (left), O2 (middle), and O3a (right) observing periods are shown.

Abbott et al. 2021a). In our analysis, we also include data around GW170608 (Abbott et al. 2017c) and GW190814 (Abbott et al. 2020e), which were released separately (Vallisneri et al. 2015; Abbott et al. 2021a). The data sets have been calibrated by the LIGO Scientific and Virgo Collaborations to convert the optical signals at the readout ports of the interferometers into time series of dimensionless strain using photon calibrator systems as length fiducials (Acernese et al. 2018; Viets et al. 2018; Bhattacharjee et al. 2021; Estevez et al. 2021). Additionally, the LIGO and Virgo data sets have undergone noise subtraction to remove persistent noise sources measured using witness auxiliary sensors (Davis et al. 2019; Estevez et al. 2019; Rolland et al. 2019; Vajente et al. 2020). Finally, data quality categories based on information of the detectors and investigations of noise sources during the observing run are provided to reduce the number of false alarms (Davis et al. 2021).

The time evolution of the BNS range for each observatory and the distribution of detector observing times are shown in Figure 1 and Table 1, respectively. In total, there have been 464 days of Advanced LIGO and Virgo observing time. Two or more detectors were observing during 320 days, of which 95 days were joint observations of the full LIGO–Hanford, LIGO–Livingston, and Virgo network.

The newly released data from O3a adds 176 days of observational data to the existing 288 days from O1 and O2. During the period of O3a, 79.7 days have data from all 3 detectors available, 68.7 days rely on a two-detector network, and 27.7 days contain data only from a single detector. Several upgrades were implemented at the LIGO and Virgo detectors between O2 and O3a to improve the sensitivity of the detectors (Abbott et al. 2021b; Buikema et al. 2020). The maximum BNS range throughout O3a was 142.4 Mpc for LIGO–Livingston, 117.2 Mpc for LIGO–Hanford, and 52.2 Mpc for Virgo.

For the first time, we also include candidates occurring during the 174 days when only one single Advanced LIGO detector was observing. We do not include single-detector candidates from the 17.4 days of Advanced Virgo data.

3. Search for Compact-binary Mergers

We use matched filtering to extract the S/N of a potential signal (Allen et al. 2012; Brown 2004), as is the standard procedure for the most sensitive gravitational-wave searches where there is an accurate model of the gravitational waveform

Table 1

Analyzed Time in Days for Different Instrument Observing Combinations

Observation	HLV	HL	HV	LV	H	L	V
O1	...	48.6	27.6	17.0	...
O2	15.2	103.3	1.7	2.2	37.8	33.0	1.7
O3a	79.7	26.1	17.4	25.2	5.6	6.4	15.7
All	95.0	178.0	19.1	27.4	70.9	56.4	17.4

Note. We use here the abbreviations H, L, and V for the LIGO–Hanford, LIGO–Livingston, and Virgo observatories, respectively. Only the indicated combination of observatories were operating for each time period, hence each is exclusive of all of the others. Some data O(1)% is excluded due to analysis requirements.

available (Messick et al. 2016; Venumadhav et al. 2020b). We assess each potential candidate for consistency with the expected gravitational-wave morphology (Allen 2005; Nitz 2018; Davies et al. 2020) and then rank potential candidates (Davies et al. 2020; Mozzon et al. 2020) based on factors including the overall noise rate and each signal’s coherence between the detectors (Nitz et al. 2017). We require a minimum S/N of 4 from each detector, which contributes to a candidate.

The procedure broadly follows the same methods used to construct the prior 2-OGC catalog (Nitz et al. 2019d), but with improvements to the removal of loud transient glitches and more stringent constraints on our suite of signal consistency tests. Detailed configuration files necessary to reproduce the analysis are included in our data release (Nitz & Capano 2021b). In addition, we use a denser bank of templates to reduce the loss in sensitivity from a mismatch between our template bank and the gravitational-wave signal. The analysis is accomplished using the public and open source PyCBC analysis toolkit (Nitz et al. 2018).

3.1. Search Space

To search for gravitational-wave sources using matched filtering, we rely on accurate models of the gravitational waveform to act as templates. To account for sources with varied component masses and component spins, we construct a discrete bank of templates designed to ensure that for any signal within the target region there is a matching template able to recover its S/N at a prescribed maximum loss. We note that different criteria would be used to maximize detections at a fixed computational cost (Allen 2021), however, this analysis is

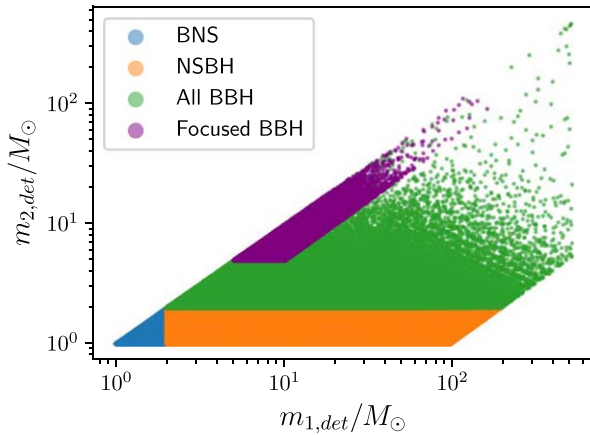


Figure 2. The detector-frame (redshifted) component masses of the templates used to search for compact-binary mergers. The template bank is constructed in four parts using stochastic placement. The BNS (blue), NSBH (orange), BBH (green), and focused BBH (purple) regions are shown. Templates in the focused BBH region are shown in purple and are bounded by $m_{1,2} > 5 M_{\odot}$, $m_1/m_2 < 2$, and $m_{1,det} + m_{2,det} < 250 M_{\odot}$. The detector-frame masses are related to the source-frame masses through the redshift (z) by $m_{1/2,det} = m_{1/2}(1+z)$, which accounts for the effects of cosmic expansion. This region is responsible for the vast majority of observed BBH mergers, but is composed of only $\sim 3\%$ of the total number of templates (~ 1.3 million), despite placement at higher density than the rest of the search space.

not computationally limited. As shown in Figure 2, the search region can be divided into three parts targeting different types of sources, namely, BNS (blue), NSBH (orange), and BBH (green and purple) sources. The template bank is designed to detect nonprecessing sources in quasi-circular orbits that can be modeled by two component masses and the spin of each component parallel to the orbital angular momentum. For BNS sources, we allow for matter effects up to $\tilde{\Lambda} < 300$, where $\tilde{\Lambda}$ is a weighted average of the component stars’ tidal deformabilities (Flanagan & Hinderer 2008). Inclusion of these effects may become important for future detectors, though they have only minor impacts on the sensitivity of current searches; we include the effect here as a proof of principle (Harry & Lundgren 2021).

The broad BNS, NSBH, and BBH regions are constructed so that signals lose no more than 3% in S/N due to the discreteness of the template bank. The boundaries are similar to those used in our previous catalog (Dal Canton & Harry 2017), however, we no longer restrict each template’s duration and instead include templates with component masses up to $500 M_{\odot}$ (detector frame). In addition, there is a separate focused BBH region (shown in purple in Figure 2) that contains the entirety of known BBH sources with the exception of the high mass-ratio merger GW190814 (Abbott et al. 2020e). To ensure the maximum sensitivity to faint signals, we place templates in this region ensuring that no more than 0.5% of the S/N is lost due to bank discreteness. Stochastic placement (Harry et al. 2009; Ajith et al. 2014) as implemented in the PyCBC toolkit (Nitz et al. 2018) is used to construct each bank.

Despite targeting nonprecessing sources, we expect this search to retain sensitivity to some types of moderately precessing sources (Abbott et al. 2016a), especially if they are short in duration or have orientation near face-on/off. Searches that neglect precession lose sensitivity to highly precessing sources if the sources are a combination of a high mass ratio, are highly inclined, and are observable for many cycles (Harry et al. 2016). Similarly, we expect this search to lose sensitivity to highly eccentric sources (Ramos-Buades

et al. 2020; Wang & Nitz 2021). Separate searches have been conducted focusing on eccentric sources (Nitz et al. 2019b; Abbott et al. 2019c; Nitz & Wang 2021a) and on those sources outside the regions we consider here (Nitz & Wang 2021b; Abbott et al. 2019a). Where the search methodology or waveform modeling is not yet sufficient, alternate techniques based on looking for coherent excess power are employed on the LIGO and Virgo data (Klimenko et al. 2008, 2016; Tiwari et al. 2016).

We employ three waveform models within our search: TaylorF2 (Sathyaprakash & Dhurandhar 1991; Droz et al. 1999; Blanchet 2002; Faye et al. 2012), IMRPhenomD (Husa et al. 2016; Khan et al. 2016), and the reduced order model of SEOBNRv4 (Taracchini et al. 2014; Bohé et al. 2017) as implemented in LALSuite (2020). TaylorF2 models only the inspiral portion of a gravitational-wave signal and is suitable for cases where the merger would be hidden by the detector noise. As such, it is employed only in the BNS region of our analysis. Where applicable, TaylorF2 includes tidal corrections up to 7.0 post-Newtonian order (Vines et al. 2011; Damour et al. 2012). IMRPhenomD is used within the focused BBH search (purple) and SEOBNRv4 is used everywhere else. Both IMRPhenomD and SEOBNRv4 model the inspiral, merger, and ringdown of a nonprecessing BBH coalescence. All models include only the dominant gravitational-wave mode. Investigations have been made in incorporating models with higher order modes into gravitational-wave searches (Capano et al. 2014; Harry et al. 2018).

3.2. Multidetector Candidates and Significance

A ranking statistic is assigned to each potential candidate following the procedure in Davies et al. (2020). The statistical significance of any given candidate is assessed by empirically estimating the rate of false alarms at the ranking statistic value associated with a candidate, and is typically reported as an inverse false-alarm rate (IFAR). The distribution of false alarms is determined by the creation of numerous analyses that do not contain astrophysical candidates (Babak et al. 2013; Usman et al. 2016). This is achieved by analyzing the data set with time offsets between the detectors large enough to break the time-of-flight requirements for a true astrophysical signal. This procedure has been used successfully in many past analyses (Abadie et al. 2012; Nitz et al. 2019d, 2019a; Abbott et al. 2019b; Venumadhav et al. 2020b; Abbott et al. 2009, 2021b). Note, however, that this method is only applicable when multiple detectors are observing.

The IFAR of the search at the ranking statistic of a given candidate, however, does not answer the question of how likely a given candidate is to be astrophysical in origin, but rather the rate at which the search will produce candidates as statistically significant under the null hypothesis. For candidates that lie in part of the parameter space where a population model can be sufficiently described, as is the case for our focused BBH region, we can predict the rate of astrophysical sources and the distribution of true astrophysical sources that would be observed by our search for a given merger rate. The response of the search to a population of sources is directly measured by adding simulated gravitational-wave signals to the data. We model the full behavior of the search using a two-component mixture model of the expected astrophysical distribution and the empirically measured distribution of false alarms (Farr et al. 2015). A similar procedure has been used in

past analyses of gravitational-wave data to assign the probability of astrophysical origin, or $\mathcal{P}_{\text{astro}}$ (Nitz et al. 2019d; Abbott et al. 2021b). For multidetector candidates that lie outside of the focused BBH region, in regions where the population of candidates is less certain or unknown, we choose not to assign a probability of astrophysical origin.

3.3. Single-detector Candidates

In this catalog, we conduct a single-detector analysis of the focused BBH and BNS regions. We rely on the methods introduced in Nitz et al. (2020) to assess the probability of astrophysical origin of the observed candidates. We assess the expected signal distribution in the same manner as for the multidetector candidates. However, due to the inability to empirically estimate the noise distribution for occurrences rarer than once per observing period, an extrapolation is needed; Nitz et al. (2020) introduce a purposefully conservative noise model for this purpose. Due to the mismatch in sensitive range between the LIGO and Virgo instruments (factor of 2–3 times), we apply the single-detector analysis to the time when a single LIGO observatory is operating, irrespective of Virgo’s observing status. In order to limit the effects of possible astrophysical contamination, we assess the background using only data collected when both LIGO observatories were observing. This ensures that most strong astrophysical signals can be excised from the data using the multidetector coincidence analysis first.

4. Parameter Inference

We infer the properties of BBH and BNS mergers by performing a Bayesian analysis with the help of PyCBC inference (Biwer et al. 2019). For BBHs, we use the latest version of the IMRPhenomXPHM waveform model (LALSuite 2020; Pratten et al. 2021), which includes subdominant harmonics and effects of precession on a quasi-circular BBH merger. In a recent study, this waveform model was used for performing parameter estimations on events from the first and second observing runs (Mateu-Lucena et al. 2021). We use the dynamical nested sampling algorithm (Skilling 2006; Higson et al. 2018), implemented in the Dynesty software package (Speagle 2020), to sample over the parameter space, which includes the chirp mass, mass ratio, spins (radial, polar, and azimuthal), distance, inclination angle, R.A., decl., coalescence phase, and the merger time. To help with sampler convergence we numerically marginalize over polarization.

For each of the events, we use uniform priors on source-frame component masses and merger time. We also assume a distance prior that is uniform in comoving volume; the luminosity distance (D_L) is related to the comoving volume assuming a flat Λ CDM cosmological model (Ade et al. 2016). An isotropic distribution of the prior in the sky localization and binary orientation is assumed for each of the events. For the spins, we use uniform priors for the magnitude of the spin and isotropic priors for the orientation.

A low-frequency cutoff (f_{low}) of 20 Hz is used for the evaluation of the likelihood function for all the detectors and for analyzing all events except for GW190727_060333 ($f_{\text{low}} = 50$ Hz for LIGO–Livingston), GW190814_211039 ($f_{\text{low}} = 30$ Hz for LIGO–Hanford; Abbott et al. 2021b), and GW190725_172728 ($f_{\text{low}} = 41$ Hz for all detectors). In some instances, the raw data contains glitches as described in Abbott et al. (2021b). Where available, we use the public glitch-subtracted data (e.g.,

GW190413_134308, GW190424_180648, GW190425_081805, GW190503_185404, GW190513_205428, GW190514_065416, GW190701_203306, and GW190924_021846; Vallisneri et al. 2015; Abbott et al. 2021a). We use 512 s of data around each candidate (with the exception of GW190725_172728) to estimate the local power spectral density (PSD) using a version of Welch’s method (Brown 2004). The data is divided into overlapping segments (8 s duration for BBH; 16 s for BNS), which are Hann-windowed. The final PSD estimate is the result of taking the mean of the median average of the odd and even segments’ power spectrum.

For GW190725_172728, only 19 s of data were available in the Hanford detector prior to the event. In order to accommodate the longest signal possible from our prior volume in this time segment, it was necessary to use a lower frequency cutoff of 41 Hz. In addition, there was a glitch in the Hanford detector at 357 s after GW190725_172728. For this reason, we restricted the PSD estimation window for the Hanford detector to 360 s for this event.

For BNS mergers, we use the IMRPhenomD_NRTidal waveform model (Khan et al. 2016; Husa et al. 2016; Dietrich et al. 2017, 2019; LALSuite 2020), which includes tidal deformability parameters Λ_1 and Λ_2 of the two component masses. We use similar priors to that of the BBH analyses on component masses, comoving volume, merger time, and orientation. We use a heterodyne method (Cornish 2010; Zackay et al. 2018; Finstad & Brown 2020) to calculate the likelihood function. For the component spins, we assume that the spins aligned with the orbital angular momentum with a magnitude of $\in [-0.05, 0.05]$. We do not assume a common equation of state for the components; instead, we allow the tidal deformability of the components $\Lambda_{1,2}$ to vary independently of each other, using a prior uniform of $\in [0, 5000]$ for both. A low-frequency cutoff of 20 Hz is used to estimate the likelihood function.

Samplers based on nested sampling algorithms make use of “live points.” These are initially drawn from the prior volume, then slowly converge toward higher likelihood regions. In the process, the sampler estimates the Bayesian evidence (Z), which is defined as the integral of the likelihood times the prior volume. We let the sampler run until the estimated remaining log-evidence is equal to a predefined value, which we set to 0.1. Where possible, we compare our results to the posteriors from previous catalogs (Nitz et al. 2019d; Abbott et al. 2019b, 2021b), considering the sampler converged if the posteriors agree up to differences expected due to the use of updated waveform models. For most events we find it sufficient to use 4000 live points. However, for a few events, it was necessary to increase the number of live points to obtain converged posteriors. For these events we increased the number of live points by 4000 until we found the posteriors to be the same between two resolutions. This resulted in between 8000 and 20000 live points used for these events.

5. Observational Results

From the combined analysis of the 2015–2019 public LIGO and Virgo data, we find 55 BBH mergers and 2 BNS mergers. The list of gravitational-wave mergers is given in Table 2. For the majority of BBHs we can assess the probability of astrophysical origin. Our catalog includes candidates where $\mathcal{P}_{\text{astro}} > 0.5$ or IFAR > 100 yr. These thresholds are consistent

Table 2
Gravitational-wave Observations from the Full Search of O1–O3a data with $\mathcal{P}_{\text{astro}} > 0.5$ or IFAR > 100 yr

Event	GPS Time	Observing	Triggered	$\mathcal{P}_{\text{astro}}$	IFAR [yr]	ρ_H	ρ_L	ρ_V	
1	GW150914_095045	1126259462.43	HL	HL	1.00	>100	19.9	13.0	...
2	GW151012_095443	1128678900.45	HL	HL	1.00	>100	6.9	6.6	...
3	GW151226_033853	1135136350.65	HL	HL	1.00	>100	10.5	7.4	...
4	GW170104_101158	1167559936.60	HL	HL	1.00	>100	8.9	9.6	...
5	GW170121_212536	1169069154.58	HL	HL	1.00	16	5.2	8.9	...
6	GW170202_135657	1170079035.73	HL	HL	0.81	0.50	5.4	6.2	...
7	GW170304_163753	1172680691.37	HL	HL	0.70	0.25	4.6	7.0	...
8	GW170403_230611	1175295989.23	HL	HL	0.71	0.25	5.2	5.5	...
9	GW170608_020116	1180922494.49	HL	HL	1.00	>100	12.4	9.0	...
10	GW170727_010430	1185152688.03	HL	HL	1.00	71	4.7	7.5	...
11	GW170729_185629	1185389807.32	HL	HL	0.99	28	7.5	6.9	...
12	GW170809_082821	1186302519.75	HLV	HL	1.00	>100	6.7	10.7	...
13	GW170814_103043	1186741861.53	HLV	HL	1.00	>100	9.2	13.7	...
14	GW170817_124104	1187008882.45	HLV	HL	...	>100	18.3	25.5	...
15	GW170818_022509	1187058327.08	HLV	HL	1.00	5.26	4.5	9.6	...
16	GW170823_131358	1187529256.52	HL	HL	1.00	>100	6.6	9.1	...
17	GW190408_181802	1238782700.28	HLV	HL	1.00	>100	9.2	10.3	...
18	GW190412_053044	1239082262.17	HLV	HL	1.00	>100	8.2	14.9	...
19	GW190413_052954	1239168612.50	HLV	HL	0.99	1.45	5.2	6.7	...
20	GW190413_134308	1239198206.74	HLV	HL	0.99	6.39	5.4	7.8	...
21	GW190421_213856	1239917954.25	HL	HL	1.00	>100	7.9	6.3	...
22	GW190424_180648	1240164426.14	L	L	0.81	9.9	...
23	GW190425_081805	1240215503.02	LV	L	0.50	11.9	...
24	GW190503_185404	1240944862.29	HLV	HL	1.00	>100	9.1	7.6	...
25	GW190512_180714	1241719652.42	HLV	HL	1.00	>100	5.9	10.8	...
26	GW190513_205428	1241816086.74	HLV	HLV	1.00	>100	8.8	7.7	4.0
27	GW190514_065416	1241852074.85	HL	HL	0.85	0.19	6.1	5.3	...
28	GW190517_055101	1242107479.83	HLV	HL	1.00	66	6.8	7.9	...
29	GW190519_153544	1242315362.38	HLV	HL	1.00	>100	7.8	9.3	...
30	GW190521_030229	1242442967.44	HLV	HL	1.00	>100	8.4	12.0	...
31	GW190521_074359	1242459857.47	HL	HL	1.00	>100	12.1	21.0	...
32	GW190527_092055	1242984073.79	HL	HL	0.93	0.37	5.0	7.0	...
33	GW190602_175927	1243533585.10	HLV	HL	1.00	>100	6.2	10.8	...
34	GW190620_030421	1245035079.31	LV	L	0.85	11.2	...
35	GW190630_185205	1245955943.18	LV	LV	1.00	0.18	...	14.7	4.0
36	GW190701_203306	1246048404.58	HLV	HLV	1.00	0.13	6.0	8.9	5.7
37	GW190706_222641	1246487219.33	HLV	HL	1.00	>100	9.4	8.6	...
38	GW190707_093326	1246527224.17	HL	HL	1.00	>100	7.9	9.6	...
39	GW190708_232457	1246663515.38	LV	L	0.85	12.6	...
40	GW190719_215514	1247608532.92	HL	HL	0.89	0.25	5.6	5.7	...
41	GW190720_000836	1247616534.71	HLV	HL	1.00	>100	6.8	7.7	...
42	GW190725_174728	1248112066.46	HLV	HL	0.91	0.41	5.4	7.3	...
43	GW190727_060333	1248242631.98	HLV	HL	1.00	>100	7.9	8.1	...
44	GW190728_064510	1248331528.53	HLV	HL	1.00	>100	7.5	10.6	...
45	GW190731_140936	1248617394.64	HL	HL	0.93	0.43	5.2	6.0	...
46	GW190803_022701	1248834439.88	HLV	HL	0.99	2.40	5.6	6.7	...
47	GW190814_211039	1249852257.01	HLV	HL	...	>100	11.0	21.1	...
48	GW190828_063405	1251009263.76	HLV	HL	1.00	>100	10.3	11.2	...
49	GW190828_065509	1251010527.89	HLV	HL	1.00	>100	7.3	7.4	...
50	GW190910_112807	1252150105.32	LV	L	0.87	13.4	...
51	GW190915_235702	1252627040.70	HLV	HL	1.00	>100	9.0	8.6	...
52	GW190916_200658	1252699636.90	HLV	HL	0.88	0.22	4.9	5.9	...
53	GW190924_021846	1253326744.84	HLV	HL	1.00	>100	6.7	10.8	...
54	GW190925_232845	1253489343.12	HV	HV	1.00	>100	8.2	...	5.4
55	GW190926_050336	1253509434.07	HLV	HL	0.88	0.27	5.4	5.6	...
56	GW190929_012149	1253755327.50	HLV	HL	0.98	3.08	5.8	7.4	...
57	GW190930_133541	1253885759.24	HL	HL	1.00	>100	6.7	7.4	...

Note. Candidates are sorted by observation time. For each candidate, we show the detectors that were observing at the time, the subset that triggered on the event within our analysis, and the S/N (ρ) reported by the search for each detector. Due to thresholds on the S/N and the ability for the search to select a preferred candidate from many at a given time, there may be no detector S/N associated with a candidate, even if it is observing at the time. For multidetector candidates, we show the false-alarm rate of the entire search at the threshold of its ranking statistic value. For BBHs found by our focused BBH search, we give estimates of the probability of astrophysical origin, $\mathcal{P}_{\text{astro}}$. We also show our estimates for single-detector candidates, which we note will necessarily be more uncertain, due to the need to extrapolate the background model. GW190425 is assessed using the same conservative extrapolation of the background as for BBH candidates, however, we expect that the noise distribution may be more well behaved than assumed here for such a long-duration signal. Candidates reported here for the first time are in bold.

with prior community conventions (Abbott et al. 2016b, 2019b; Nitz et al. 2019a, 2019d; Venumadhav et al. 2020a). The marginalized parameter estimates for source-frame component masses, chirp mass, mass ratio, effective spin, luminosity

distance, redshift, final mass, and the final spin obtained from the posterior distributions are listed in Table 4.

Several candidates were independently detected by Virgo, with the Virgo observatory being decisive in the case of two of

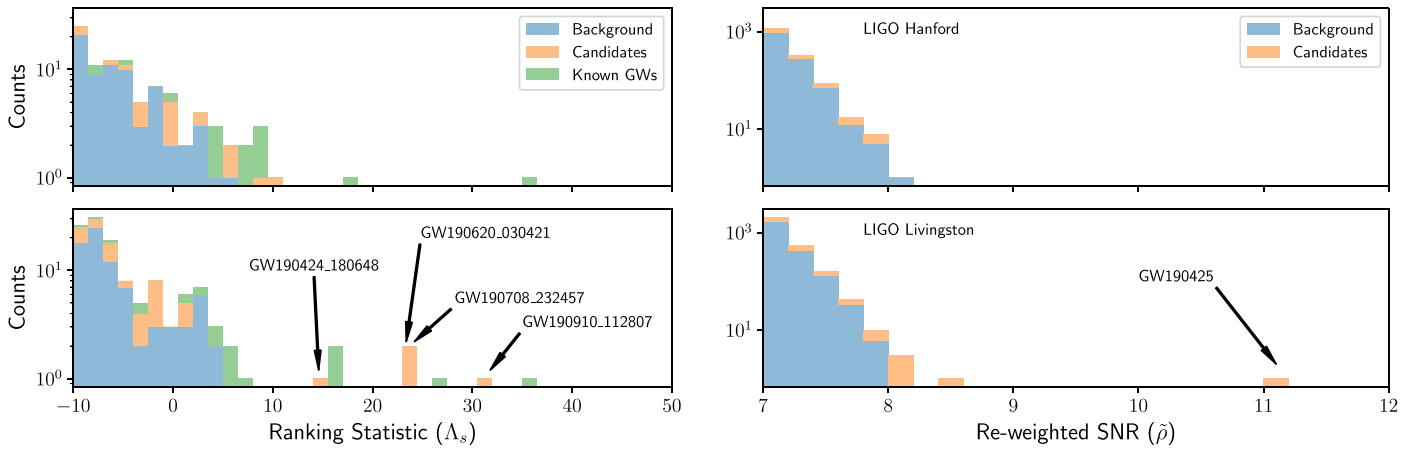


Figure 3. The stacked distributions of single-detector triggered candidates observed when a single LIGO observatory was operating (green), our selected background (blue), and for comparison the distribution of gravitational-wave mergers observed by the multidetector analysis (orange) as a function of the ranking statistic. To estimate the significance of the candidates, the method of Nitz et al. (2020) is used to extrapolate the background distribution, which allows us to estimate the probability of astrophysical origin. Shown are the results of the BBH analysis (left), which uses the statistic λ , (Nitz et al. 2020), and BNS analysis (right), which uses a reweighted S/N statistic (Babak et al. 2013; Nitz et al. 2019d), for the LIGO–Hanford (top) and LIGO–Livingston (bottom) data during O3a.

them. As the gap in sensitivity between the LIGO and Virgo instruments narrows, we expect this to become more commonplace. We identify four candidates in our single-detector analysis of BNS and BBH mergers in LIGO–Hanford and LIGO–Livingston data as shown in Figure 3. These are consistent with the previously reported single-detector analysis of Abbott et al. (2021b).

We find four previously unreported BBH mergers, in which three of them, GW190725_174728, GW190916_200658, and GW190926_050336 are near-threshold observations with relatively low S/N, and the fourth, GW190925_232845, has an S/N of ~ 10 and is found at a false-alarm rate $< 1/100$ yr. We find that GW190925_232845 has component masses $20.2^{+3.9}_{-2.3} M_{\odot}$ and $15.6^{+2.1}_{-2.6} M_{\odot}$. While not reported as a new BBH merger detection, this time was noted as part of a recent search for lensed images (McIsaac et al. 2020; Abbott et al. 2021d). The remainder of the multidetector observed mergers are broadly consistent with previous searches (Venumadhav et al. 2020a; Abbott et al. 2021b, 2019b). Two marginal observations reported in Abbott et al. (2021b), 190426_152155 and 190909_114149, are not assigned high significance in our analysis, but notably, our updated catalog now includes two candidates that were originally reported in Venumadhav et al. (2020a) from O2, GW170202_135657 and GW170403_230611.

5.1. Binary Black Holes

The mass and spin distributions of the observed population of gravitational-wave mergers, along with their localization posteriors, can be used to constrain various formation channels or population synthesis models (O’Shaughnessy et al. 2008; Stevenson et al. 2015; Zevin et al. 2021) and to estimate the rate of mergers (Roulet et al. 2020; Abbott et al. 2021c). In Figure 4 we show the one-dimensional marginal posteriors on the component masses, effective spin, and luminosity distance for our observed BBH population. Figure 5 shows the combined posterior for all our observed BBH sources, with and without accounting for the zeroth order selection effect

introduced by the variation of signal loudness as a function of intrinsic source parameters.

To estimate the source population, we combine the posterior samples for the component masses from each event to obtain one large collection of mass samples. We do not make additional assumptions about the mass prior and redshift distribution of the population apart from the priors used in parameter estimation. To account for signal loudness, we assign a weight to each sample in the combined posterior that is inversely proportional to the comoving volume that corresponds to the horizon distance of the given sample. The horizon distance is defined as the maximum luminosity distance an optimally oriented source can be detected with a single-detector threshold S/N of 8.

5.1.1. GW190521

GW190521_030229 (GW190521) is the most massive confident detection in our catalog. Initial parameter estimates produced by the LIGO and Virgo Collaborations indicated that its component masses were $85^{+21}_{-14} M_{\odot}$ and $66^{+17}_{-18} M_{\odot}$ (Abbott et al. 2020c, 2020d). This would put at least one of the objects in the upper mass gap caused by pair-instability supernovae (PISN; Woosley 2017; Marchant et al. 2019; Stevenson et al. 2019; van Son et al. 2020), suggesting that the event may have been created by a hierarchical merger (Fragione et al. 2020; Kimball et al. 2021; Liu & Lai 2021). This interpretation was challenged in Nitz & Capano (2021a) who found multiple modes in the mass posterior. The additional modes were at a larger mass ratio (extending to $q \sim 6$ or $q \sim 10$, depending on the waveform model used), such that component masses straddled the PISN mass gap. However, the highest mass-ratio mode (at $q \sim 10$) was found by an earlier version of the IMRPhenomXPHM model. An updated version of the IMRPhenomXPHM model (as used in this work) better accounts for the possibility that the total angular momentum could flip direction, inducing transitional precession. With the corrected version of IMRPhenomXPHM, we no longer find significant support for the mass ratio of $q \sim 10$, however support for the mode at $q \sim 6$ remains. This is consistent with the findings of Estellés et al. (2021).

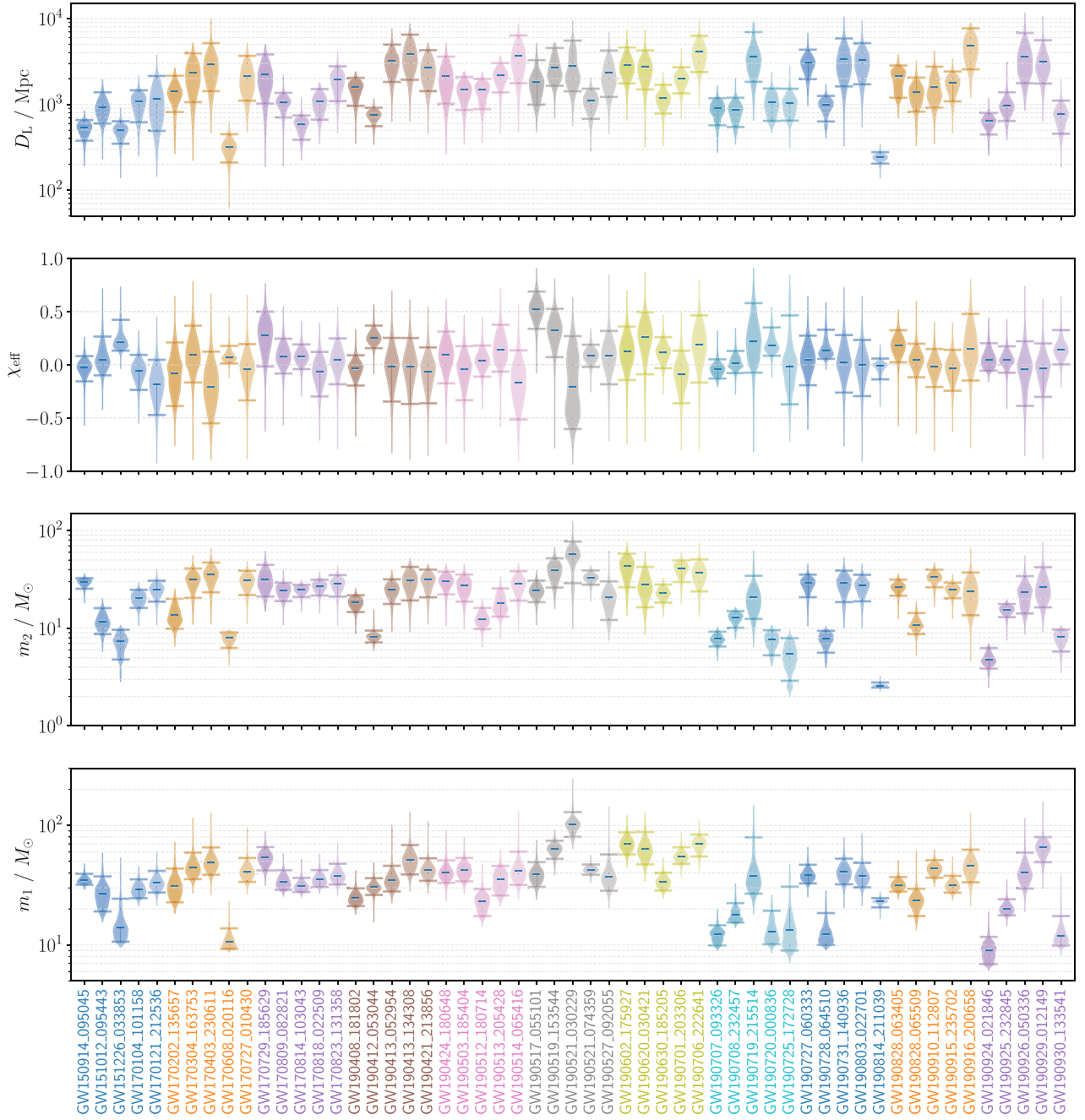


Figure 4. The marginalized distributions for component masses m_1 , m_2 , the effective spin χ_{eff} , and the luminosity distance D_L for all BBH events detected in 3-OGC. The median value and the 5th and 95th quantile values are marked with a bar, respectively. Different colors are used to aid associating each event with its posterior estimates.

An analysis using ringdown quasi-normal modes performed in Capano et al. (2021) has shown the more equal-mass scenario, however, may be unlikely. The analysis found strong observational evidence for the presence of the $(1m) = (330)$ subdominant harmonic. That a nonzero amplitude was detected for the (330) quasi-normal mode indicates that GW190521 may not be an equal-mass binary.

An electromagnetic counterpart was detected by the Zwicky Transient Factory that may be from the same source as GW190521 (Graham et al. 2020). If so, this would suggest that GW190521 occurred in the accretion disk of an active galactic nuclei. Nitz & Capano (2021a) found only marginal support for the event to be in coincidence with the electromagnetic signal,

with a log Bayes factor of -4 – 2.3 . Using the updated version of IMRPhenomXPHM gives a log Bayes factor of -3.8 – 2.5 .

5.1.2. Other Multimodal Events

In addition to GW190521, we find three other events that show second peaks in the likelihood at more asymmetric mass ratios, GW151226_033853 (GW151226), GW190620_030421, and GW190725_172728. However, the prior (which is uniform in component masses) disfavors the higher mass ratio. In addition, for GW190725_172728 the asymmetric mass portion of the posterior is correlated with a second peak in effective spin at $\chi_{\text{eff}} \sim 0.5$, which is also disfavored by assuming a spin prior that is isotropic in orientation. The combination of the prior and

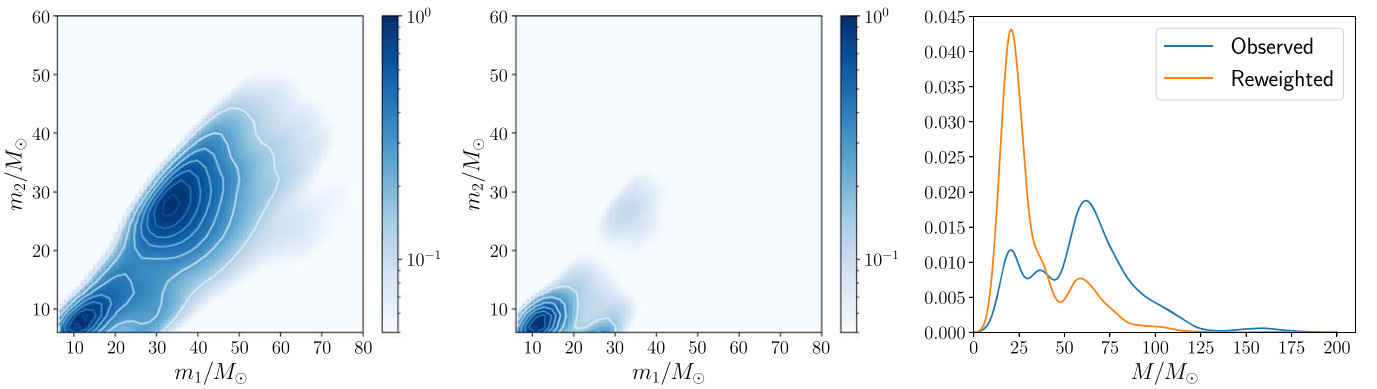


Figure 5. Distribution of the source-frame masses of the BBH population from the posteriors obtained from a parameter estimation run on all of the detected BBH events. Here we show the detected component mass distribution (left), the component mass distribution corrected for the zeroth order selection effect (middle), and the one-dimensional marginals of the total mass distribution (right). The middle plot assumes a constant detection threshold and corrects the distribution for the effect of the signal loudness varying with component mass.

Table 3
The Selection of Subthreshold Candidates with $\mathcal{P}_{\text{astro}} > 0.2$ or IFAR > 0.5 from the Full Search of O1–O3a Data

Event	GPS Time	Observing	Triggered	$\mathcal{P}_{\text{astro}}$	IFAR	ρ_H	ρ_L	ρ_V	$m_{1,\text{det}}/M_\odot$	$m_{2,\text{det}}/M_\odot$	χ_{eff}	
1	151011_192749	1128626886.60	HL	HL	0.21	0.02	4.7	6.8	...	33.5	65.6	0.1
2	151205_195525	1133380542.41	HL	HL	0.25	0.03	5.9	4.8	...	81.6	77.7	0.1
3	170425_055334	1177134832.19	HL	HL	0.41	0.07	5.3	5.8	...	46.1	65.0	0.1
4	170704_202003	1183234821.62	HL	HL	0.34	0.05	5.1	6.5	...	10.0	13.2	-0.0
5	170722_065503	1184741721.32	HL	HL	...	0.89	5.0	7.3	...	1.7	1.3	-0.0
6	190404_142514	1238423132.99	HL	HL	0.44	0.02	5.1	5.9	...	22.5	24.5	0.1
7	190426_053949	1240292407.21	HLV	HL	0.32	0.01	5.2	6.1	...	20.7	20.0	0.2
8	190427_180650	1240423628.68	HLV	HL	0.41	0.02	5.8	6.8	...	13.0	7.9	-0.0
9	190509_004120	1241397698.79	HLV	HL	0.31	0.01	4.7	6.2	...	30.1	28.2	-0.0
10	190524_134109	1242740487.36	HLV	HL	0.21	0.01	4.3	6.0	...	123.3	77.2	0.2
11	190530_030659	1243220837.97	HLV	HL	0.31	0.01	5.2	5.8	...	26.3	45.4	0.2
12	190630_135302	1245938000.49	HL	HL	0.23	0.01	5.1	5.8	...	32.6	19.2	0.0
13	190704_104834	1246272532.92	HLV	HL	0.26	0.01	7.0	5.5	...	5.0	5.4	0.1
14	190707_071722	1246519060.10	HLV	HL	0.21	0.01	6.0	5.7	...	10.7	14.1	0.0
15	190805_105432	1249037690.78	HL	HL	0.41	0.02	4.8	6.5	...	9.4	18.3	-0.1
16	190808_230535	1249340753.59	HLV	HL	0.31	0.01	5.0	6.5	...	13.6	13.6	0.2
17	190821_050019	1250398837.88	HLV	HL	0.23	0.01	5.2	5.6	...	26.8	17.0	-0.1

Note. Candidates are sorted by the observation time. The complete set of subthreshold candidates is available in the data release and includes a selection of full parameter estimates. Here we show the detector-frame (redshifted) parameters of the template that triggered on the candidate, along with the reported S/Ns (ρ) from each detector.

the lower S/Ns of GW190620_030421 and GW190725_17272 results in a weak multimodal structure in the component mass marginal posterior that is less pronounced than it is for GW190521.

A large uncertainty in the mass ratio of GW151226 was found by Mateu-Lucena et al. (2021) using the same waveform model. More recently, a bimodal distribution in the masses of GW151226 was reported by Chia et al. (2021), again using the same waveform model. However, Chia et al. (2021) found larger support at more asymmetric masses than we do, as well as a secondary peak in the chirp mass for which we find weak support. Determining whether these events have a truly larger mass ratio than previously expected, or if these secondary modes are due to systematic errors in waveform modeling, will require more study.

5.1.3. High Mass Ratio Mergers

The events with the largest (unambiguous) mass ratio are GW190814_211039 (GW190814) and GW190412_053044 (GW190412), with mass ratios of $m_1/m_2 = 8.9^{+1.1}_{-1.5}$ and $3.7^{+1.4}_{-0.9}$,

respectively. These estimates are consistent with those found by the LIGO and Virgo Collaborations (Abbott et al. 2020g, 2020e). The smaller object in GW190814 had a mass of $2.6^{+0.2}_{-0.1} M_\odot$, making it either the least massive black hole or the most massive neutron star ever detected. If it is a neutron star, it should have a nonzero (albeit small) tidal deformability. Unfortunately, given the high mass ratio and the low S/N, the event cannot bound the tidal deformability away from zero (Flanagan & Hinderer 2008), making it ambiguous whether the object was a neutron star or a black hole (Abbott et al. 2020e). These two events were also the first to have measurable power in subdominant harmonics, the $(l, m) = (3, 3)$ mode for both (Abbott et al. 2020g, 2020e), which can be used to test general relativity as in Capano & Nitz (2020).

5.2. Neutron Star Binaries

The only observed neutron star binaries remain the previously reported GW170817 (Abbott et al. 2017a) and GW190425 (Abbott et al. 2020a). The latter is observed in only the LIGO–Livingston data, but given its separation from the background, and the long duration of the signal which increases the power of signal

Table 4
Bayesian Parameter Estimation for the 57 Detections in the Entire O1–O3a Data

Event	m_1/M_\odot	m_2/M_\odot	\mathcal{M}/M_\odot	q	χ_{eff}	D_L/Mpc	z	M_f/M_\odot	χ_f	S/N
1	$34.7^{+4.7}_{-2.8}$	$29.8^{+2.8}_{-4.4}$	$27.9^{+1.4}_{-1.3}$	$1.2^{+0.4}_{-0.1}$	$-0.03^{+0.11}_{-0.13}$	534^{+123}_{-157}	$0.11^{+0.02}_{-0.03}$	$61.5^{+2.9}_{-2.7}$	$0.67^{+0.03}_{-0.05}$	23.8
2	$27.0^{+10.5}_{-3.1}$	$11.8^{+4.3}_{-3.1}$	$15.2^{+1.1}_{-0.9}$	$2.3^{+2.0}_{-1.1}$	$0.05^{+0.22}_{-0.15}$	927^{+456}_{-329}	$0.18^{+0.08}_{-0.06}$	$37.4^{+2.7}_{-3.8}$	$0.62^{+0.08}_{-0.08}$	9.8
3	$14.1^{+10.3}_{-3.4}$	$7.4^{+2.2}_{-2.6}$	$8.8^{+0.2}_{-0.2}$	$1.9^{+3.2}_{-0.2}$	$0.22^{+0.21}_{-0.08}$	503^{+133}_{-156}	$0.11^{+0.03}_{-0.03}$	$20.5^{+7.9}_{-1.5}$	$0.72^{+0.03}_{-0.03}$	13.2
4	$29.1^{+6.3}_{-4.4}$	$20.5^{+4.2}_{-4.3}$	$21.0^{+1.9}_{-1.5}$	$1.4^{+0.7}_{-0.4}$	$-0.06^{+0.15}_{-0.18}$	1077^{+384}_{-458}	$0.21^{+0.07}_{-0.08}$	$47.5^{+4.2}_{-3.3}$	$0.65^{+0.06}_{-0.09}$	13.7
5	$33.0^{+8.7}_{-5.6}$	$25.1^{+6.4}_{-6.4}$	$24.9^{+3.7}_{-3.2}$	$1.3^{+0.3}_{-0.3}$	$-0.19^{+0.29}_{-0.29}$	1164^{+673}_{-673}	$0.23^{+0.12}_{-0.12}$	$55.9^{+7.9}_{-7.0}$	$0.61^{+0.08}_{-0.13}$	10.9
6	$17.7^{+12.6}_{-8.2}$	$13.7^{+6.3}_{-3.8}$	$17.5^{+3.1}_{-1.5}$	$2.3^{+2.1}_{-1.1}$	$-0.08^{+0.29}_{-0.31}$	1422^{+735}_{-608}	$0.27^{+0.12}_{-0.11}$	$43.6^{+9.7}_{-5.6}$	$0.54^{+0.17}_{-0.15}$	8.5
7	$44.5^{+14.7}_{-9.6}$	$31.7^{+9.3}_{-11.2}$	$32.1^{+6.8}_{-5.7}$	$1.4^{+1.3}_{-0.3}$	$0.1^{+0.27}_{-0.26}$	2354^{+1584}_{-1293}	$0.42^{+0.22}_{-0.21}$	$72.4^{+15.0}_{-10.8}$	$0.7^{+0.09}_{-0.13}$	8.7
8	$49.1^{+16.4}_{-10.5}$	$35.8^{+11.4}_{-12.4}$	$35.9^{+8.7}_{-6.7}$	$1.3^{+1.1}_{-0.3}$	$-0.21^{+0.33}_{-0.33}$	2967^{+2204}_{-1540}	$0.51^{+0.29}_{-0.24}$	$81.4^{+19.0}_{-14.0}$	$0.6^{+0.11}_{-0.17}$	7.7
9	$10.6^{+3.1}_{-1.3}$	$8.0^{+1.1}_{-1.1}$	$8.0^{+0.2}_{-0.2}$	$1.3^{+0.9}_{-0.3}$	$0.07^{+0.11}_{-0.06}$	321^{+129}_{-110}	$0.07^{+0.03}_{-0.02}$	$17.8^{+1.5}_{-0.6}$	$0.69^{+0.02}_{-0.03}$	15.2
10	$41.3^{+12.1}_{-7.6}$	$30.8^{+10.0}_{-8.9}$	$30.7^{+5.5}_{-4.6}$	$1.3^{+0.3}_{-0.3}$	$-0.04^{+0.23}_{-0.3}$	2153^{+529}_{-1050}	$0.39^{+0.22}_{-0.17}$	$69.1^{+11.9}_{-9.7}$	$0.66^{+0.08}_{-0.14}$	8.8
11	$53.8^{+12.1}_{-11.8}$	$31.6^{+13.0}_{-10.4}$	$35.1^{+7.9}_{-5.8}$	$1.7^{+1.1}_{-0.6}$	$0.28^{+0.22}_{-0.29}$	2236^{+1590}_{-1215}	$0.4^{+0.23}_{-0.2}$	$80.9^{+15.0}_{-11.0}$	$0.76^{+0.08}_{-0.16}$	10.8
12	$33.9^{+8.2}_{-5.0}$	$24.5^{+4.7}_{-3.5}$	$24.9^{+2.1}_{-1.6}$	$1.4^{+0.8}_{-0.3}$	$0.08^{+0.16}_{-0.15}$	1069^{+293}_{-364}	$0.21^{+0.05}_{-0.07}$	$55.8^{+4.3}_{-3.3}$	$0.69^{+0.08}_{-0.08}$	12.4
13	$30.9^{+5.4}_{-3.2}$	$24.9^{+2.9}_{-4.0}$	$24.0^{+1.3}_{-1.0}$	$1.2^{+0.5}_{-0.2}$	$0.07^{+0.12}_{-0.12}$	593^{+149}_{-207}	$0.12^{+0.03}_{-0.04}$	$53.2^{+3.0}_{-2.3}$	$0.7^{+0.04}_{-0.04}$	17.4
14	$1.4^{+0.1}_{-0.1}$	$1.3^{+0.1}_{-0.1}$	$1.186^{+0.003}_{-0.001}$	$1.1^{+0.2}_{-0.1}$	$-0.0^{+0.01}_{-0.01}$	43^{+5}_{-10}	$0.01^{+0.0}_{-0.0}$	32.7
15	$35.2^{+7.1}_{-9.4}$	$27.0^{+4.4}_{-4.4}$	$26.7^{+1.9}_{-1.9}$	$1.3^{+0.6}_{-0.3}$	$-0.07^{+0.19}_{-0.19}$	1073^{+414}_{-414}	$0.21^{+0.07}_{-0.07}$	$59.6^{+4.7}_{-4.0}$	$0.65^{+0.07}_{-0.09}$	11.8
16	$38.1^{+9.7}_{-6.0}$	$28.6^{+6.4}_{-7.5}$	$28.4^{+4.2}_{-3.1}$	$1.3^{+0.8}_{-0.3}$	$0.05^{+0.12}_{-0.23}$	1965^{+810}_{-873}	$0.36^{+0.12}_{-0.14}$	$63.5^{+9.0}_{-6.3}$	$0.69^{+0.07}_{-0.11}$	11.4
17	$24.5^{+5.2}_{-3.4}$	$18.4^{+3.4}_{-3.7}$	$18.3^{+1.8}_{-1.5}$	$1.3^{+0.6}_{-0.3}$	$-0.04^{+0.13}_{-0.16}$	1585^{+447}_{-625}	$0.3^{+0.07}_{-0.11}$	$41.1^{+3.9}_{-2.7}$	$0.66^{+0.05}_{-0.07}$	14.0
18	$30.4^{+5.8}_{-4.2}$	$8.2^{+2.2}_{-1.1}$	$13.2^{+0.5}_{-0.3}$	$3.7^{+1.9}_{-0.4}$	$0.25^{+0.11}_{-0.1}$	757^{+56}_{-200}	$0.15^{+0.03}_{-0.04}$	$37.5^{+4.9}_{-3.2}$	$0.65^{+0.04}_{-0.03}$	19.1
19	$34.7^{+11.2}_{-6.7}$	$25.1^{+6.7}_{-7.3}$	$25.4^{+4.8}_{-3.7}$	$1.4^{+1.0}_{-0.3}$	$-0.02^{+0.27}_{-0.33}$	3193^{+1784}_{-1366}	$0.54^{+0.24}_{-0.2}$	$57.3^{+10.7}_{-7.9}$	$0.66^{+0.09}_{-0.15}$	9.0
20	$51.6^{+16.9}_{-12.7}$	$31.2^{+11.4}_{-11.9}$	$34.1^{+7.5}_{-6.9}$	$1.6^{+1.6}_{-0.9}$	$-0.01^{+0.23}_{-0.3}$	3835^{+2665}_{-1869}	$0.63^{+0.34}_{-0.22}$	$79.4^{+16.0}_{-13.9}$	$0.64^{+0.11}_{-0.09}$	9.9
21	$42.2^{+8.8}_{-7.8}$	$31.4^{+8.5}_{-10.6}$	$31.1^{+6.0}_{-5.1}$	$1.3^{+1.1}_{-0.3}$	$-0.06^{+0.33}_{-0.27}$	2679^{+1605}_{-1251}	$0.47^{+0.22}_{-0.19}$	$70.1^{+12.3}_{-9.8}$	$0.65^{+0.08}_{-0.15}$	9.9
22	$40.2^{+10.9}_{-9.4}$	$30.7^{+7.3}_{-8.4}$	$30.3^{+5.1}_{-4.2}$	$1.3^{+0.8}_{-0.3}$	$0.09^{+0.22}_{-0.27}$	2134^{+1466}_{-1115}	$0.38^{+0.21}_{-0.19}$	$67.6^{+10.9}_{-9.3}$	$0.7^{+0.12}_{-0.12}$	10.3
23	$1.8^{+0.2}_{-0.1}$	$1.5^{+0.1}_{-0.1}$	$1.432^{+0.013}_{-0.013}$	$1.2^{+0.2}_{-0.2}$	$0.02^{+0.02}_{-0.02}$	174^{+46}_{-43}	$0.04^{+0.01}_{-0.01}$	12.4
24	$42.5^{+10.9}_{-8.5}$	$27.5^{+8.1}_{-8.7}$	$29.2^{+4.8}_{-3.9}$	$1.5^{+1.2}_{-0.5}$	$-0.04^{+0.22}_{-0.29}$	1478^{+608}_{-619}	$0.28^{+0.1}_{-0.11}$	$66.9^{+10.0}_{-7.3}$	$0.64^{+0.09}_{-0.18}$	12.2
25	$23.2^{+6.1}_{-5.8}$	$12.5^{+3.6}_{-2.7}$	$14.6^{+1.4}_{-1.4}$	$1.9^{+1.1}_{-0.8}$	$0.04^{+0.14}_{-0.13}$	1499^{+481}_{-618}	$0.28^{+0.08}_{-0.08}$	$34.4^{+4.3}_{-3.3}$	$0.65^{+0.06}_{-0.07}$	12.0
26	$35.2^{+10.7}_{-9.3}$	$18.1^{+7.4}_{-5.0}$	$21.5^{+3.4}_{-2.2}$	$1.9^{+0.9}_{-0.4}$	$0.14^{+0.23}_{-0.21}$	2195^{+833}_{-815}	$0.39^{+0.13}_{-0.13}$	$51.4^{+8.1}_{-6.4}$	$0.69^{+0.11}_{-0.13}$	12.0
27	$41.4^{+18.8}_{-9.7}$	$28.9^{+9.6}_{-9.7}$	$29.8^{+7.6}_{-5.7}$	$1.4^{+1.3}_{-0.4}$	$-0.17^{+0.35}_{-0.35}$	3704^{+2662}_{-1939}	$0.61^{+0.34}_{-0.28}$	$67.8^{+18.5}_{-12.5}$	$0.6^{+0.11}_{-0.18}$	8.1
28	$38.8^{+10.5}_{-8.2}$	$24.4^{+6.4}_{-5.8}$	$26.6^{+2.2}_{-3.6}$	$1.6^{+0.9}_{-0.5}$	$0.52^{+0.16}_{-0.19}$	1839^{+438}_{-847}	$0.34^{+0.14}_{-0.14}$	$59.6^{+8.2}_{-8.2}$	$0.85^{+0.04}_{-0.07}$	11.4
29	$63.7^{+10.7}_{-11.2}$	$39.7^{+12.4}_{-13.6}$	$43.0^{+7.0}_{-7.6}$	$1.6^{+1.1}_{-0.5}$	$0.32^{+0.2}_{-0.25}$	2669^{+1877}_{-1021}	$0.46^{+0.26}_{-0.16}$	$97.7^{+12.8}_{-12.4}$	$0.76^{+0.08}_{-0.12}$	13.6
30	$101.7^{+27.6}_{-21.4}$	$57.6^{+19.6}_{-28.7}$	$64.9^{+12.1}_{-14.2}$	$1.8^{+2.8}_{-0.6}$	$-0.21^{+0.48}_{-0.4}$	2833^{+2705}_{-1412}	$0.49^{+0.36}_{-0.22}$	$152.0^{+25.5}_{-17.0}$	$0.54^{+0.21}_{-0.17}$	15.2
31	$42.7^{+4.4}_{-4.0}$	$33.2^{+5.9}_{-5.3}$	$32.6^{+2.8}_{-2.4}$	$1.3^{+0.3}_{-0.2}$	$0.09^{+0.1}_{-0.11}$	1112^{+410}_{-434}	$0.22^{+0.07}_{-0.08}$	$72.1^{+5.4}_{-4.4}$	$0.7^{+0.04}_{-0.04}$	24.4
32	$37.5^{+19.7}_{-9.1}$	$20.9^{+9.3}_{-8.7}$	$23.6^{+6.7}_{-3.7}$	$1.8^{+2.6}_{-0.7}$	$0.09^{+0.23}_{-0.27}$	2340^{+1903}_{-1119}	$0.42^{+0.27}_{-0.18}$	$56.3^{+17.2}_{-8.6}$	$0.67^{+0.11}_{-0.24}$	8.7
33	$70.6^{+16.9}_{-13.4}$	$43.6^{+14.4}_{-17.3}$	$47.3^{+8.4}_{-8.7}$	$1.6^{+0.5}_{-0.5}$	$0.12^{+0.24}_{-0.27}$	2897^{+1145}_{-1145}	$0.5^{+0.17}_{-0.17}$	$108.8^{+15.7}_{-13.8}$	$0.69^{+0.16}_{-0.16}$	12.2
34	$63.5^{+24.7}_{-16.2}$	$28.0^{+14.5}_{-11.1}$	$35.9^{+7.7}_{-6.9}$	$2.3^{+2.6}_{-1.1}$	$0.26^{+0.23}_{-0.35}$	2721^{+1538}_{-1228}	$0.47^{+0.21}_{-0.19}$	$88.5^{+19.4}_{-12.9}$	$0.72^{+0.11}_{-0.12}$	12.0
35	$33.7^{+6.5}_{-5.2}$	$23.0^{+5.1}_{-4.7}$	$24.0^{+2.3}_{-1.5}$	$1.5^{+0.7}_{-0.5}$	$0.12^{+0.14}_{-0.15}$	1192^{+498}_{-409}	$0.23^{+0.08}_{-0.07}$	$54.3^{+4.2}_{-3.3}$	$0.7^{+0.05}_{-0.09}$	15.3
36	$55.2^{+10.6}_{-7.4}$	$41.2^{+8.4}_{-11.4}$	$41.0^{+5.0}_{-4.8}$	$1.3^{+0.8}_{-0.3}$	$-0.09^{+0.22}_{-0.28}$	2015^{+691}_{-671}	$0.37^{+0.1}_{-0.11}$	$91.9^{+10.0}_{-8.4}$	$0.64^{+0.08}_{-0.11}$	11.8
37	$70.2^{+13.6}_{-15.2}$	$37.0^{+13.7}_{-13.1}$	$43.0^{+9.1}_{-7.2}$	$1.9^{+1.4}_{-0.7}$	$0.19^{+0.28}_{-0.35}$	4111^{+2188}_{-1730}	$0.66^{+0.28}_{-0.24}$	$101.4^{+16.3}_{-12.5}$	$0.71^{+0.11}_{-0.22}$	12.6
38	$12.2^{+2.4}_{-2.3}$	$7.8^{+1.4}_{-1.3}$	$8.4^{+0.3}_{-0.3}$	$1.6^{+0.5}_{-0.5}$	$-0.04^{+0.09}_{-0.09}$	901^{+278}_{-332}	$0.18^{+0.06}_{-0.06}$	$19.1^{+1.2}_{-1.2}$	$0.64^{+0.03}_{-0.03}$	12.8
39	$17.8^{+4.5}_{-2.4}$	$13.0^{+2.0}_{-2.9}$	$13.2^{+0.7}_{-0.7}$	$1.4^{+0.8}_{-0.3}$	$0.01^{+0.12}_{-0.09}$	873^{+322}_{-329}	$0.18^{+0.06}_{-0.06}$	$29.5^{+2.4}_{-1.6}$	$0.67^{+0.03}_{-0.05}$	12.7
40	$38.0^{+41.5}_{-11.2}$	$20.7^{+13.8}_{-8.2}$	$23.6^{+17.1}_{-10.8}$	$1.8^{+2.7}_{-0.3}$	$0.22^{+0.36}_{-0.3}$	3607^{+3356}_{-1776}	$0.6^{+0.42}_{-0.26}$	$55.9^{+46.0}_{-11.2}$	$0.72^{+0.13}_{-0.2}$	7.9
41	$12.9^{+6.4}_{-2.8}$	$7.7^{+1.9}_{-2.4}$	$8.6^{+0.6}_{-0.5}$	$1.7^{+1.9}_{-0.6}$	$0.18^{+0.17}_{-0.17}$	1055^{+475}_{-413}	$0.21^{+0.08}_{-0.08}$	$19.8^{+4.2}_{-1.9}$	$0.71^{+0.03}_{-0.04}$	10.7
42	$13.4^{+1.3}_{-4.4}$	$5.5^{+2.4}_{-2.6}$	$7.3^{+0.6}_{-0.5}$	$2.4^{+8.3}_{-1.3}$	$-0.02^{+0.48}_{-0.35}$	1035^{+487}_{-389}	$0.2^{+0.08}_{-0.07}$	$18.3^{+4.9}_{-2.6}$	$0.58^{+0.13}_{-0.11}$	9.5
43	$38.4^{+8.5}_{-5.6}$	$29.1^{+6.3}_{-8.3}$	$28.7^{+3.4}_{-3.4}$	$1.3^{+0.3}_{-0.3}$	$0.05^{+0.22}_{-0.24}$	3102^{+1236}_{-1132}	$0.53^{+0.17}_{-0.17}$	$64.0^{+9.0}_{-6.4}$	$0.69^{+0.08}_{-0.11}$	11.4
44	$12.2^{+6.2}_{-2.2}$	$7.8^{+1.6}_{-2.2}$	$8.5^{+0.5}_{-0.3}$	$1.6^{+1.7}_{-0.5}$	$0.13^{+0.2}_{-0.08}$	1000^{+255}_{-368}	$0.2^{+0.04}_{-0.07}$	$19.2^{+4.2}_{-1.1}$	$0.7^{+0.02}_{-0.04}$	12.7
45	$40.9^{+11.9}_{-8.7}$	$29.4^{+9.6}_{-10.8}$	$29.5^{+7.1}_{-5.8}$	$1.4^{+1.2}_{-0.3}$	$0.02^{+0.26}_{-0.29}$	3345^{+2523}_{-1726}	$0.56^{+0.33}_{-0.26}$	$66.7^{+14.4}_{-11.2}$	$0.68^{+0.09}_{-0.16}$	8.1
46	$37.6^{+11.1}_{-7.2}$	$27.5^{+7.8}_{-8.6}$	$27.5^{+5.7}_{-4.2}$	$1.3^{+1.0}_{-0.3}$	$-0.0^{+0.24}_{-0.29}$	3289^{+1882}_{-1574}	$0.55^{+0.25}_{-0.23}$	$62.0^{+12.1}_{-8.7}$	$0.67^{+0.08}_{-0.15}$	8.5
47	$23.1^{+1.6}_{-1.4}$	$2.6^{+0.2}_{-0.1}$	$6.1^{+0.1}_{-0.1}$	$8.9^{+1.1}_{-1.5}$	$-0.01^{+0.07}_{-0.13}$	241^{+37}_{-37}	$0.05^{+0.01}_{-0.01}$	$25.4^{+1.5}_{-2.2}$	$0.27^{+0.03}_{-0.06}$	25.1
48	$31.8^{+3.9}_{-3.9}$	$26.6^{+5.0}_{-5.0}$	$25.0^{+3.7}_{-2.1}$	$1.2^{+0.2}_{-0.2}$	$0.18^{+0.16}_{-0.16}$	2120^{+719}_{-925}	$0.38^{+0.15}_{-0.15}$	$54.9^{+7.6}_{-4.4}$	$0.74^{+0.06}_{-0.06}$	15.8
49	$23.5^{+6.0}_{-6.0}$	$10.9^{+3.4}_{-2.2}$	$13.7^{+1.3}_{-1.0}$	$2.2^{+1.1}_{-0.9}$	$0.05^{+0.15}_{-0.16}$	1393^{+657}_{-573}	$0.27^{+0.11}_{-0.1}$	$33.2^{+4.6}_{-4.0}$	$0.63^{+0.06}_{-0.08}$	11.1
50	$43.5^{+7.7}_{-7.0}$	$33.5^{+6.4}_{-7.2}$	$33.0^{+3.9}_{-3.9}$	$1.3^{+0.5}_{-0.3}$	$-0.02^{+0.17}_{-0.17}$	1609^{+1139}_{-694}	$0.3^{+0.17}_{-0.12}$	$73.5^{+8.1}_{-8.3}$	$0.67^{+0.06}_{-0.08}$	13.5
51	$31.6^{+6.3}_{-4.2}$	$25.0^{+4.3}_{-4.6}$	$24.2^{+2.8}_{-1.9}$	$1.2^{+0.5}_{-0.2}$	$-0.03^{+0.17}_{-0.21}$	1778^{+642}_{-693}	$0.33^{+0.11}_{-0.12}$	$54.0^{+5.8}_{-4.2}$	$0.66^{+0.06}_{-0.08}$	13.2
52	$45.7^{+17.0}_{-12.3}$	$24.0^{+13.2}_{-10.4}$	$28.0^{+9.0}_{-6.4}$	$1.8^{+2.2}_{-0.8}$	$0.15^{+0.34$					

consistency tests (Usman et al. 2016), we consider this detection robust. We obtain a slightly higher estimate for the effective spin of GW190425 than what was reported in Abbott et al. (2020a). This is due to a difference in the prior: as stated above, we use a prior uniform in the spin-component aligned with the orbital angular momentum, whereas Abbott et al. (2020a) used a prior on the spin that was isotropic in orientation. Reweighting our posterior to a prior isotropic in orientation yields the same effective spin as reported in Abbott et al. (2020a). We find all other parameters of GW190425 and GW170817 to be consistent with the low-spin prior results reported in Abbott et al. (2020a) and Abbott et al. (2019d).

GW170817 is the only merger unambiguously observed by electromagnetic emission (Abbott et al. 2017b). Due to the possibility of electromagnetic emission from neutron star mergers, we encourage the use of subthreshold BNS and NSBH candidates released with this catalog to investigate correlations with other archival observations and potentially detect faint sources.

5.3. Subthreshold Candidates

In Table 3 we show the 17 subthreshold candidates with $\mathcal{P}_{\text{astro}} > 0.2$ or $\text{IFAR} > 0.5$. Several subthreshold candidates have been previously identified. In particular, 151205_195525 was included in 2-OGC as a near-threshold observation; in our updated analysis it is reduced in significance. 170425_055334 was previously reported in Venumadhav et al. (2020). 151011_192749 was reported in 2-OGC as a subthreshold event. The majority of these subthreshold candidates are consistent with BBH mergers. However, 170722_065503 is consistent with a BNS merger. The full data release includes subthreshold candidates at lower significance throughout the searched parameter space.

From visual inspection of the time-frequency representations of the data around these candidates, there are no signs of loud noise transients that could have caused the corresponding triggers. In a few instances, minor excess power can be observed at frequencies between 50 and 100 Hz, or at lower frequencies. We cannot conclude if any of these minor power signatures correspond to an instrumental noise artifact or to a marginal astrophysical signal.

6. Data Release

We provide analysis configurations, metadata, and results at <https://github.com/gwastro/3-ogc> (Nitz & Capano 2021b). The files contain $\mathcal{O}(10^6)$ subthreshold candidates along with their time, S/N, and values for various signal consistency tests. Details of the signal consistency tests and how they are to be interpreted are given in Nitz (2018) and Allen (2005). Each candidate event lists the associated false-alarm rate and ranking statistic to assess their significance. For the most significant candidates inside the focused BBH region discussed in Section 3.2 we provide an estimate of the probability of astrophysical origin, $\mathcal{P}_{\text{astro}}$. We also release our Bayesian parameter inference posterior samples for each of the candidates shown in Table 4, along with a selection of subthreshold candidates. Additional data products and intermediate results may be made available upon request.




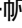



7. Conclusions

The 3-OGC catalog of gravitational-wave mergers covers the complete observing period from 2015 to 2019 and includes

BNS, NSBH, and BBH candidates. For the first time we include candidates observed by a single sensitive detector. 3-OGC contains the most comprehensive set of merger candidates, including a total of 57 gravitational-wave observations in this period. This includes four single-detector mergers in addition to the four BBH mergers reported here for the first time. We find no additional BNS or NSBH detections beyond the previously reported GW170817 and GW190425. Only the first half of the O3 run, which concluded in 2020, has been made public. As the data from the latter half of the observing run is not yet released, the catalog here covers only O1, O2, and O3a. We expect the second half of O3, O3b, to be released in six months, at which point an updated catalog will be produced.

We thank Bruce Allen and Duncan Brown for providing useful comments. We are grateful to the computing team from AEI Hannover for their significant technical support. M.C. acknowledges funding from the Natural Sciences and Engineering Research Council of Canada (NSERC). This research has made use of data from the Gravitational Wave Open Science Center (<https://www.gw-openscience.org>), a service of LIGO Laboratory, the LIGO Scientific Collaboration, and the Virgo Collaboration. LIGO is funded by the U.S. National Science Foundation. Virgo is funded by the French Centre National de Recherche Scientifique (CNRS), the Italian Istituto Nazionale della Fisica Nucleare (INFN), and the Dutch Nikhef, with contributions by Polish and Hungarian institutes.

ORCID iDs

Alexander H. Nitz  <https://orcid.org/0000-0002-1850-4587>
 Collin D. Capano  <https://orcid.org/0000-0002-0355-5998>
 Sumit Kumar  <https://orcid.org/0000-0002-6404-0517>
 Yi-Fan Wang (王一帆)  <https://orcid.org/0000-0002-2928-2916>
 Shilpa Kastha  <https://orcid.org/0000-0003-0966-1748>
 Marlin Schäfer  <https://orcid.org/0000-0002-6990-0627>
 Rahul Dhurkunde  <https://orcid.org/0000-0002-5077-8916>
 Miriam Cabero  <https://orcid.org/0000-0003-4059-4512>

References

- Aasi, J., Abbott, B. P., Abbott, R., et al. 2015, *CQGra*, 32, 074001
 Abadie, J., Abbott, B. P., Abbott, R., et al. 2012, *PhRvD*, 85, 082002
 Abbott, B. P., Abbott, R., Abbott, T. D., et al. 2016a, *PhRvD*, 93, 122003
 Abbott, B. P., Abbott, R., Abbott, T. D., et al. 2016b, *PhRvX*, 6, 041015
 Abbott, B. P., Abbott, R., Abbott, T. D., et al. 2017a, *ApJL*, 848, L12
 Abbott, B. P., Abbott, R., Abbott, T. D., et al. 2017c, *ApJL*, 851, L35
 Abbott, B. P., Abbott, R., Abbott, T. D., et al. 2019b, *PhRvX*, 9, 031040
 Abbott, B. P., Abbott, R., Abbott, T. D., et al. 2019c, *ApJ*, 883, 149
 Abbott, B. P., Abbott, R., Abbott, T. D., et al. 2019d, *PhRvX*, 9, 011001
 Abbott, B., Abbott, R., Abbott, T. D., et al. 2009, *PhRvD*, 80, 047101
 Abbott, B., Abbott, R., Abbott, T. D., et al. 2017a, *PhRvL*, 119, 161101
 Abbott, B., Abbott, R., Abbott, T. D., et al. 2019a, *PhRvL*, 123, 161102
 Abbott, B., Abbott, R., Abbott, T. D., et al. 2020a, *ApJL*, 892, L3
 Abbott, R., Abbott, T. D., Abraham, S., et al. 2021a, *SoftX*, 13, 100658
 Abbott, R., Abbott, T. D., Abraham, S., et al. 2021b, *PhRvX*, 11, 021503
 Abbott, R., Abbott, T. D., Abraham, S., et al. 2020c, *PhRvL*, 125, 101102
 Abbott, R., Abbott, T. D., Abraham, S., et al. 2020d, *ApJL*, 900, L13
 Abbott, R., Abbott, T. D., Abraham, S., et al. 2020e, *ApJL*, 896, L44
 Abbott, R., Abbott, T. D., Abraham, S., et al. 2021c, *ApJL*, 913, L7
 Abbott, R., Abbott, T. D., Abraham, S., et al. 2020g, *PhRvD*, 102, 043015
 Abbott, R., Abbott, T. D., Abraham, S., et al. 2021d, *arXiv:2105.06384*
 Acernese, F., Agathos, M., Agatsuma, K., et al. 2015, *CQGra*, 32, 024001
 Acernese, F., Adams, T., Agatsuma, K., et al. 2018, *CQGra*, 35, 205004
 Ade, P. A. R., Aghanim, N., Arnaud, M., et al. 2016, *A&A*, 594, A13
 Ajith, P., Fotopoulos, N., Privitera, S., Neunzert, A., & Weinstein, A. J. 2014, *PhRvD*, 89, 084041

- Allen, B. 2005, *PhRvD*, **71**, 062001
- Allen, B. 2021, *PhRvD*, **104**, 042005
- Allen, B., Anderson, W. G., Brady, P. R., Brown, D. A., & Creighton, J. D. E. 2012, *PhRvD*, **85**, 122006
- Andreoni, I., Anand, S., Bianco, F. B., et al. 2019, *PASP*, **131**, 068004
- Babak, S., Biswas, R., Brady, P., et al. 2013, *PhRvD*, **87**, 024033
- Bhattacharjee, D., Lecoche, Y., Karki, S., et al. 2021, *CQGra*, **38**, 015009
- Biwer, C. M., Capano, C. D., De, S., et al. 2019, *PASP*, **131**, 024503
- Blanchet, L. 2002, *LRR*, **5**, 3
- Bohé, A., Shao, L., Taracchini, A., et al. 2017, *PhRvD*, **95**, 044028
- Brown, D. A. 2004, PhD thesis, University of Wisconsin-Milwaukee
- Buikema, A., Cahillane, C., Mansell, G. L., et al. 2020, *PhRvD*, **102**, 062003
- Burns, E., Goldstein, A., Hui, C. M., et al. 2019, *ApJ*, **871**, 90
- Capano, C., Pan, Y., & Buonanno, A. 2014, *PhRvD*, **89**, 102003
- Capano, C. D., Cabero, M., Abedi, J., et al. 2021, arXiv:2105.05238
- Capano, C. D., & Nitz, A. H. 2020, *PhRvD*, **102**, 124070
- Chia, H. S., Olsen, S., Roulet, J., et al. 2021, Boxing Day Surprise: Higher Multipoles and Orbital Precession in GW151226, arXiv:2105.06486
- Cornish, N. J. 2010, arXiv:1007.4820
- Countryman, S., Keivani, A., Bartos, I., et al. 2019, arXiv:1901.05486
- Dal Canton, T., & Harry, I. W. 2017, arXiv:1705.01845
- Damour, T., Nagar, A., & Villain, L. 2012, *PhRvD*, **85**, 123007
- Davies, G. S., Dent, T., Tápai, M., et al. 2020, *PhRvD*, **102**, 022004
- Davis, D., Massinger, T. J., Lundgren, A. P., et al. 2019, *CQGra*, **36**, 055011
- Davis, D., Areeda, J. S., Berger, B. K., et al. 2021, *CQGra*, **38**, 135014
- Dietrich, T., Bernuzzi, S., & Tichy, W. 2017, *PhRvD*, **96**, 121501
- Dietrich, T., Khan, S., Dudi, R., et al. 2019, *PhRvD*, **99**, 024029
- Droz, S., Knapp, D. J., Poisson, E., & Owen, B. J. 1999, *PhRvD*, **59**, 124016
- Eidelman, B., Doctor, Z., & Farr, B. 2021, *ApJL*, **913**, L23
- Estellés, H., Husa, S., Colleoni, M., et al. 2021, arXiv:2105.06360
- Estevez, D., Lagabbe, P., Masserot, A., et al. 2021, *CQGra*, **38**, 075007
- Estevez, D., Mours, B., Rolland, L., & Verkindt, D. 2019, Online h(t) reconstruction for Virgo O3 data: start of O3, Tech. Rep. VIR-0652B-19, Virgo
- Farr, W. M., Gair, J. R., Mandel, I., & Cutler, C. 2015, *PhRvD*, **91**, 023005
- Faye, G., Marsat, S., Blanchet, L., & Iyer, B. R. 2012, *CQGra*, **29**, 175004
- Finstad, D., & Brown, D. A. 2020, *ApJL*, **905**, L9
- Flanagan, E. E., & Hinderer, T. 2008, *PhRvD*, **77**, 021502
- Fragione, G., Loeb, A., & Rasio, F. A. 2020, *ApJL*, **902**, L26
- Gayathri, V., Healy, J., Lange, J., et al. 2020, arXiv:2009.05461
- Gerosa, D., & Fishbach, M. 2021, *NatAs*, **5**, 749
- Graham, M. J., Ford, K. E. S., McKernan, B., et al. 2020, *PhRvL*, **124**, 251102
- Harry, I., Calderón Bustillo, J., & Nitz, A. 2018, *PhRvD*, **97**, 023004
- Harry, I., & Lundgren, A. 2021, *PhRvD*, **104**, 043008
- Harry, I., Privitera, S., Bohé, A., & Buonanno, A. 2016, *PhRvD*, **94**, 024012
- Harry, I. W., Allen, B., & Sathyaprakash, B. 2009, *PhRvD*, **80**, 104014
- Higson, E., Handley, W., Hobson, M., & Lasenby, A. 2018, *Statistics and Computing*, **29**, 891
- Husa, S., Khan, S., Hannam, M., et al. 2016, *PhRvD*, **93**, 044006
- Khan, S., Husa, S., Hannam, M., et al. 2016, *PhRvD*, **93**, 044007
- Kimball, C., Talbot, C., Berry, C. P. L., et al. 2021, *ApJL*, **915**, L35
- Klimenko, S., Yakushin, I., Mercer, A., & Mitselmakher, G. 2008, *CQGra*, **25**, 114029
- Klimenko, S., Vedovato, G., Drago, M., et al. 2016, *PhRvD*, **93**, 042004
- LALSuite. 2020, LSC Algorithm Library Suite, <https://git.ligo.org/lscsoft/lalsuite>
- Liu, B., & Lai, D. 2021, *MNRAS*, **502**, 2049
- Marchant, P., Renzo, M., Farmer, R., et al. 2019, *ApJ*, **882**, 36
- Mateu-Lucena, M., Husa, S., Colleoni, M., et al. 2021, Adding harmonics to the interpretation of the black hole mergers of GWTC-1, arXiv:2105.05960
- Mclsaac, C., Keitel, D., Collett, T., et al. 2020, *PhRvD*, **102**, 084031
- Messick, C., Blackburn, K., Brady, P., et al. 2016, *PhRvD*, **95**, 042001
- Mozzon, S., Nuttall, L. K., Lundgren, A., et al. 2020, *CQGra*, **37**, 215014
- Nitz, A. H. 2018, *CQGra*, **35**, 035016
- Nitz, A. H., Capano, C., Nielsen, A. B., et al. 2019a, *ApJ*, **872**, 195
- Nitz, A. H., & Capano, C. D. 2021a, *ApJL*, **907**, L9
- Nitz, A. H., Capano, C. D., et al. 2021b, 3-OGC Open Gravitational-wave Catalog, www.github.com/gwastro/3-ogc, GitHub
- Nitz, A. H., Dent, T., Dal Canton, T., Fairhurst, S., & Brown, D. A. 2017, *ApJ*, **849**, 118
- Nitz, A. H., Dent, T., Davies, G. S., et al. 2019d, *ApJ*, **891**, 123
- Nitz, A. H., Dent, T., Davies, G. S., & Harry, I. 2020, *ApJ*, **897**, 169
- Nitz, A. H., Harry, I. W., Willis, J. L., et al. 2018, PyCBC Software, <https://github.com/gwastro/pycbc>, GitHub
- Nitz, A. H., Lenon, A., & Brown, D. A. 2019b, *ApJ*, **890**, 1
- Nitz, A. H., Nielsen, A. B., & Capano, C. D. 2019c, *ApJL*, **876**, L4
- Nitz, A. H., & Wang, Y.-F. 2021a, *ApJ*, **915**, 54
- Nitz, A. H., & Wang, Y.-F. 2021b, *PhRvL*, **126**, 021103
- O'Shaughnessy, R., Kim, C., Kalogera, V., & Belczynski, K. 2008, *ApJ*, **672**, 479
- Pratten, G., García-Quirós, C., Colleoni, M., et al. 2021, *PhRvD*, **103**, 104056
- Ramos-Buades, A., Tiwari, S., Haney, M., & Husa, S. 2020, *PhRvD*, **102**, 043005
- Rolland, L., Seglar-Arroyo, M., & Verkindt, D. 2019, Reprocessing of h(t) for the last two weeks of O3a, Tech. Rep. VIR-1201A-19, Virgo
- Romero-Shaw, I. M., Lasky, P. D., Thrane, E., & Bustillo, J. C. 2020, *ApJL*, **903**, L5
- Roulet, J., Venumadhav, T., Zackay, B., Dai, L., & Zaldarriaga, M. 2020, *PhRvD*, **102**, 123022
- Sathyaprakash, B. S., & Dhurandhar, S. V. 1991, *PhRvD*, **44**, 3819
- Setzer, C. N., Biswas, R., Peiris, H. V., et al. 2019, *MNRAS*, **485**, 4260
- Skilling, J. 2006, *BayAn*, **1**, 833
- Speagle, J. S. 2020, *MNRAS*, **493**, 3132
- Stevenson, S., Ohme, F., & Fairhurst, S. 2015, *ApJ*, **810**, 58
- Stevenson, S., Sampson, M., Powell, J., et al. 2019, *ApJ*, **882**, 121
- Taracchini, A., Buonanno, A., Pan, Y., et al. 2014, *PhRvD*, **89**, 061502
- Tiwari, V., Klimenko, S., Christensen, N., et al. 2016, *PhRvD*, **93**, 043007
- Usman, S. A., Nitz, A. H., Harry, I. W., et al. 2016, *CQGra*, **33**, 215004
- Vajente, G., Huang, Y., Isi, M., et al. 2020, *PhRvD*, **101**, 042003
- Vallisneri, M., Kanner, J., Williams, R., Weinstein, A., & Stephens, B. 2015, *J. Phys. Conf. Ser.*, **610**, 012021
- van Son, L., de Mink, S., Broekgaarden, F., et al. 2020, *ApJ*, **897**, 100
- Venumadhav, T., Zackay, B., Roulet, J., Dai, L., & Zaldarriaga, M. 2020a, *PhRvD*, **101**, 083030
- Venumadhav, T., Zackay, B., Roulet, J., Dai, L., & Zaldarriaga, M. 2020b, *PhRvD*, **100**, 023011
- Viets, A., et al. 2018, *CQGra*, **35**, 095015
- Vines, J., Flanagan, E. E., & Hinderer, T. 2011, *PhRvD*, **83**, 084051
- Wang, Y.-F., & Nitz, A. H. 2021, *ApJ*, **912**, 53
- Woosley, S. E. 2017, *ApJ*, **836**, 244
- Zackay, B., Dai, L., & Venumadhav, T. 2018, Relative Binning and Fast Likelihood Evaluation for Gravitational Wave Parameter Estimation, arXiv:1806.08792
- Zevin, M., Bavera, S. S., Berry, C. P. L., et al. 2021, *ApJ*, **910**, 152